Author for correspondence:
Eva Kanso
e-mail: kanso@usc.edu

Cilia oscillations

Yi Man, Feng Ling and Eva Kanso

Department of Aerospace and Mechanical Engineering, University of Southern California, Los Angeles, CA 90089, USA

(iD) FL, 0000-0002-1766-073X; EK, 0000-0003-0336-585X

Cilia, or eukaryotic flagella, are microscopic active filaments expressed on the surface of many eukaryotic cells, from single-celled protozoa to mammalian epithelial surfaces. Cilia are characterized by a highly conserved and intricate internal structure in which molecular motors exert forces on microtubule doublets causing cilia oscillations. The spatial and temporal regulations of this molecular machinery are not well understood. Several theories suggest that geometric feedback control from cilium deformations to molecular activity is needed. Here, we implement a recent sliding control model, where the unbinding of molecular motors is dictated by the sliding motion between microtubule doublets. We investigate the waveforms exhibited by the model cilium, as well as the associated molecular motor dynamics, for hinged and clamped boundary conditions. Hinged filaments exhibit base-to-tip oscillations while clamped filaments exhibit both base-to-tip and tip-to-base oscillations. We report the change in oscillation frequencies and amplitudes as a function of motor activity and sperm number, and we discuss the validity of these results in the context of experimental observations of cilia behaviour.

This article is part of the Theo Murphy meeting issue 'Unity and diversity of cilia in locomotion and transport'.

1. Introduction

Eukaryotic cilia and flagella are driven into oscillatory motion by an intricate internal structure, referred to as the axoneme (figure 1). The axoneme structure, composed of microtubule doublets and dynein molecular motors, is highly conserved across evolutionary time and cell type [1,2]. However, the mechanisms that regulate the activity of the molecular motors, causing them to produce oscillatory motions, remain elusive. At present, there is no universal, experimentally tested theory for describing the active forces and moments generated in the axoneme that lead to sustained cilia oscillations.

Details of the structure of the axoneme of motile cilia were first delineated by transmission electron microscopy in the middle of the twentieth century [2]. The axoneme consists of nine microtubule doublets, connected to a central pair of microtubules via radial spokes, which is known as the '9+2' structure as shown in figure 1. Nexin links connect the outer microtubule doublets. During their power stroke, outer and inner dynein arms bind to neighbouring microtubules, generating equal and opposite forces on adjacent microtubule doublets. Unbinding of the dynein stalk requires energy—the energy released by the hydrolysis of ATP. The key unresolved problem is the spatial and temporal regulation of the binding and unbinding of molecular motors and its bearing on the oscillations of the cilium.

Several experimental approaches have been proposed to address this problem [3–12]. Rapid freezing of live cilia samples by sudden removal of ATP result in rigour waves [4], and reactivation of these waves with reintroduction of ATP shows wave propagation towards the flagellum tip as if oscillations had not been interrupted [5,13]. These results, in conjunction with other experiments on the functions of dynein motors [14], suggest that cilia oscillations are in tight control of the molecular machinery. By contrast, during experimentation with low concentrations of ATP in the algae model system *Chlamydomonas reinhardtii*, flagella were observed to bend at almost constant curvature, suggesting a static
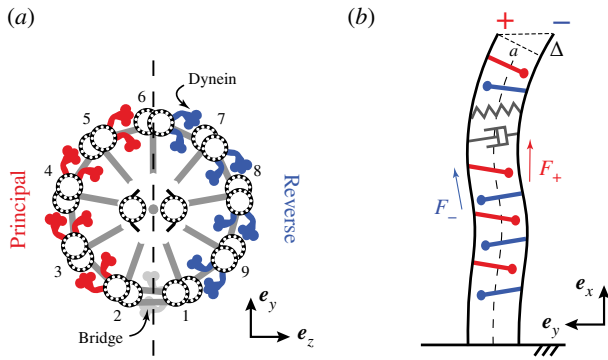
Figure 1. Axoneme structure. (*a*) The cross section of a typical cilium. Dynein motors between microtubule doublets induce sliding, which gets resisted by elastic links. A symmetry-breaking bridge between two doublets separates the dynein motors into principal (red) and reverse (blue) sides. (*b*) Model cilium consists of two elastic filaments (+ and −) coupled by elastic linker and damper, with dynein motors exerting sliding forces (F_+ and F_-) on different sides of the cilium. The bending of the cilium results in a relative sliding Δ between + and − filaments. (Online version in colour.)

mode that is distinct from the dynamic beating mode [11,15]. Reactivation of the dynamic mode was possible with gradual increase of ATP. The relaxed configurations observed at low ATP and the transition to oscillatory motions with increasing levels of ATP suggest that oscillations could be induced by a mechanical instability that does not require fine spatio-temporal regulation of the molecular motors.

Rapid freezing methods were recently coupled to powerful cryogenic electron microscopy to provide detailed structures of the conformations of the molecular motors [7–9,12]. Snapshots of the dynein conformations at various instances of the cilium beating cycle were then correlated with the overall waveform of the cilium to draw experimentally based hypotheses on the regulation of the molecular motors in relation to cilia oscillations [12]. Asymmetrical activation of the dynein motors correlates with local curvature, suggesting that reciprocal inhibition is likely the main mechanism of dynein control at full waveform beating. These results support the notion that oscillations are finely controlled by the molecular motors [12], but they do not rule out the existence of an 'open-loop' instability mechanism that triggers the onset of oscillations.

Existing theories designed to shed light on the mechanisms controlling the molecular machinery either assume *geometric feedback control* from the cilium configuration to the molecular motor activity [16–29], or, more recently, rely on *steady distributed axial forces* where the dynein activity need not be affected by the cilium configuration [30–32].

Geometric feedback theories come in three flavours: sliding control, curvature control or geometric clutch. The key idea in the sliding control theory is that the activity of molecular motors, and thus the active forces they generate, is regulated by the tangential sliding distance between two adjacent microtubule doublets caused by the bending motion of the axoneme [19,33,34]. The curvature control theory considers that the magnitude of the active forces is proportional to the curvature of the centreline of the axoneme [17,18], whereas the geometric clutch approach considers the active forces to be governed by the separation distances between adjacent doublets [21,22,35]. Comparison of these three feedback mechanisms suggests that curvature control gives best-fits to experimentally observed waveforms [36,37].

However, regulation of dynein activity may not be required to generate oscillatory motions [30–32,38]. Oscillations arise as a result of a dynamic buckling instability—a Hopf bifurcation—induced by the axial stresses applied by the dynein motors on the axoneme. These mechanisms are particularly appealing because they provide a simpler explanation for sustained oscillations that does not require fine tuning of the molecular motor activity, but they do not explain the differential dynein binding observed in Lin & Nicastro [12].

Mathematical models, whether in support of feedback control or instability-driven oscillations, are an abstraction of the axoneme structure, ignoring several details in favour of analytical representations of the cilium centreline. These models are motivated by the fact that the '9+2' axoneme is characterized by a bridge that connects two adjacent doublets, labelled 1 and 2 in figure 1, thus dividing the dynein motors into principal (P) and reverse (R) sides relative to the bridge. Motors on the two sides operate antagonistically resulting in cilia oscillations. This 'tug-of-war' aspect of the motor activity is minimally captured in the context of two elastic filaments (+) and (−) of length L, representing opposite sides of the axonemal bridge and separated by a constant distance a at their base. The (±) filaments are subject to an active force doublet that results in an active moment density m_a on the centreline, allowing it to deform in the plane of motion, as shown in figure 1.

In this study, we implement a hierarchical model adapted from Oriola *et al.* [39], and recently analysed in Chakrabarti & Saintillan [40], that couples the centreline dynamics to a microscopic model of the motor activity. We reproduce the results of Chakrabarti & Saintillan [40] for clamped filaments, and we extend their analysis of travelling wave direction to hinged filaments: hinged filaments always exhibit wave propagation from base-to-tip, while clamped filaments exhibit both base-to-tip and tip-to-base oscillations. In hinged filaments, we observe that molecular activities form sharp propagation fronts while the filament oscillates smoothly. For clamped filaments, in addition to the analysing direction of wave propagation over the parameter space of motor activity and sperm number as done in Chakrabarti & Saintillan [40], we analyse in detail the change in amplitude and frequency of oscillations over the same parameter space. We observe sharp transitions in both amplitude and frequency across the lines marking the change in wave direction. We conclude by comparing these trends to experimental observations of cilia behaviour.

2. Mathematical formulation

The cilium centreline is described by $\mathbf{r}(s, t)$, where s is the arc length measured from the base and t is time. The positions of the (±) filaments are given by $\mathbf{r}_\pm(s, t) = \mathbf{r}(s, t) \pm \frac{a}{2}\mathbf{n}$, where $\mathbf{n}(s, t)$ is the unit normal along the centreline and a is the separation distance between the ± filaments. We also introduce the unit tangent $\mathbf{t}(s, t)$ to the centreline. In a Cartesian coordinate, say (x,y) whose origin is located at the base of the centreline, we write $\mathbf{t} = [\cos\theta, \sin\theta]$, and $\mathbf{n} = [-\sin\theta, \cos\theta]$, where $\tan\theta(s, t) = \partial y/\partial x$ is the local slope of the centreline, and $\mathbf{r} = [x(s, t), y(s, t)]$.

The equations of motion of the centreline that arise from balancing the tangential and normal forces and bending moments, including the moment due to motor activity [19,35,41,42], are given by

$$\mathbf{F}_s + \mathbf{f}_\mathrm{h} = \mathbf{0} \qquad (2.1)$$

and

$$M_s + N + m_a = 0, \tag{2.2}$$

where $\mathbf{f}_h$ is the hydrodynamic force per unit length, m_a is the active moment per unit length, $\mathbf{F} = \sigma\mathbf{t} + N\mathbf{n}$ and M are the internal forces and moment acting along the centreline, with σ and N denoting the tangential and normal components of the internal force. The notation $\mathbf{F}_s = \partial\mathbf{F}/\partial s$ and $M_s = \partial M/\partial s$ is used to represent the spatial derivatives with respect to s.

Due to the slenderness of the filament ($a \ll L$), we model the hydrodynamic force using the resistive force theory at low Reynolds number (e.g. [43,44]). That is, we consider $\mathbf{f}_h$ to be proportional to the local velocity with anisotropic drag coefficients

$$\mathbf{f}_h = -(\xi_\parallel \mathbf{tt} + \xi_\perp \mathbf{nn}) \cdot \mathbf{r}_t, \tag{2.3}$$

where $\mathbf{r}_t = \partial\mathbf{r}/\partial t$ represents the time derivative. The drag coefficients satisfy $\xi_\perp = 2\xi_\parallel$ with $\xi_\perp = 4\pi\mu/\ln(L/a)$. A more accurate representation of the hydrodynamic forces in terms of the slender-body theory (e.g. [45–48]), which includes the algebraic corrections with non-local hydrodynamic interactions, was considered in Chakrabarti & Saintillan [40].

Equation (2.1) can be written in scalar form as follows. Substitute $\mathbf{F} = \sigma\mathbf{t} + N\mathbf{n}$ and (2.3) into (2.1) and multiply both sides with $(\xi_\parallel^{-1}\mathbf{tt} + \xi_\perp^{-1}\mathbf{nn})$ to obtain the following representation of the filament velocity:

$$\mathbf{r}_t = \xi_\parallel^{-1}(\sigma_s - N\theta_s)\mathbf{t} + \xi_\perp^{-1}(\sigma\theta_s + N_s)\mathbf{n}. \tag{2.4}$$

Here, we have substituted $\mathbf{t}_s = \theta_s\mathbf{n}$ and $\mathbf{n}_s = -\theta_s\mathbf{t}$. Now, assume the filament is not extensible and apply the constraint $\mathbf{r}_{ts} \cdot \mathbf{r}_s = 0$ to get, upon introducing $\gamma = \xi_\parallel/\xi_\perp$,

$$\sigma_{ss} - (1 + \gamma)N_s\theta_s - N\theta_{ss} - \gamma\sigma\theta_s^2 = 0 \tag{2.5}$$

and

$$N_{ss} - \gamma^{-1}N\theta_s^2 + (1 + \gamma^{-1})\sigma_s\theta_s + \sigma\theta_{ss} = \xi_\perp\theta_t. \tag{2.6}$$

Equation (2.2) is simplified further by considering a linear constitutive relation for the bending moment $M = B\theta_s$, where B is the bending rigidity. Substituting into equation (2.2), we have

$$B\theta_{ss} + N + m_a = 0. \tag{2.7}$$

Equations (2.5)–(2.7) provide a set of three coupled partial differential equations that we use to solve for $\sigma(s, t)$, $N(s, t)$ and $\theta(s, t)$, subject to properly chosen boundary conditions. Here, we consider one end of the filament to be either clamped or hinged at the wall, that is, at $s = 0$, and the other end to be free. The force- and moment-free boundary conditions at $s = L$ are given by

$$\sigma|_{s=L} = 0, \quad N|_{s=L} = 0 \quad \text{and} \quad B\theta_s|_{s=L} = 0. \tag{2.8}$$

At the wall, from $\mathbf{r}_t(s = 0, t) = 0$, we get

$$(\sigma_s - N\theta_s)|_{s=0} = 0 \quad \text{and} \quad (\sigma\theta_s + N_s)|_{s=0} = 0. \tag{2.9}$$

If, in addition, we assume that the filament is clamped, we have

$$\theta|_{s=0} = 0. \tag{2.10}$$

However, if the filament is hinged, the total moment at $s = 0$

vanishes, leading to

$$B\theta_s|_{s=0} - \int_0^L m_a(s', t)\,\mathrm{d}s' = 0. \tag{2.11}$$

The filament dynamics can thus be obtained by solving equations (2.5)–(2.7) subject to the six boundary conditions in equations (2.8), (2.9) and either (2.10) for the clamped case or (2.11) for the hinged case.

In the limit of small deformations $\theta(s, t)$, we see from (2.5) and (2.6) that $N \sim O(\theta)$ while $\sigma \sim O(\theta^2)$. Therefore, the tension σ is negligible. We can cancel the normal force N by substituting equation (2.7) into (2.6), leading to a single governing equation of the form (see appendix A)

$$\xi_\perp\theta_t = -B\theta_{ssss} - (m_a)_{ss}. \tag{2.12}$$

We will use the linearized equation in (2.12) to probe the linear stability of the straight filament.

The active moment m_a per unit length is generated by the longitudinal force doublets $f(s, t)$ per unit length that represent the effects of the molecular motor activity

$$m_a(s, t) = af(s, t). \tag{2.13}$$

As the centreline deforms and bends under the influence of m_a, it induces relative sliding Δ between the two ($\pm$) filaments where the internal forces $f(s, t)$ are applied (figure 1). The relative sliding $\Delta = \int_0^s [|(\mathbf{r}_-)_s| - |(\mathbf{r}_+)_s|]\,\mathrm{d}\tilde{s}$ is given by

$$\Delta(s, t) = a[\theta(s, t) - \theta(0, t)]. \tag{2.14}$$

This sliding is resisted by cross-linker proteins that act as a linear spring of stiffness K. This sliding resistance is crucial to account for complex passive dynamics of the axoneme [49–52]. In other words, the internal force density f consists of active and passive parts, arising from both the motor activity and the passive response of the nexin cross-linkers [39,40]

$$f(s, t) = \rho(n_+F_+ + n_-F_-) - K\Delta. \tag{2.15}$$

Here, ρ is the average density of motors along both filaments, $n_\pm$ are the fractions of motors on the ($\pm$) filaments that are in the bound state, $F_\pm$ is the load exerted by a single motor. To close the model in (2.15), we must model the binding kinetics of the molecular motors as well as the motor loads. For the binding kinetics, we use a common two-state mechanochemical model consisting of bound and unbound molecular motors, with a constant total (bound or unbound) number of motors on both filaments. A single motor can bind to the opposite filament at a rate π and unbind at a rate ε. We assume that the motors switch between these two states stochastically; then, the fractions $n_\pm$ of attached and detached motors follow the Fokker–Planck evolution equations

$$(n_\pm)_t = \pi(1 - n_\pm) - \epsilon n_\pm. \tag{2.16}$$

In earlier works [16,19,53], the exchange rates π and ε depend on periodic potential landscapes that govern the interaction of the molecular motors with the filaments. A simpler model was proposed recently in Oriola et al. [39] based on experimental measurements; in this empirical model, the binding rate $\pi = \pi_o$ is constant and the unbinding rate ε exponentially increases with the load $F_\pm$ exerted by the motor, $\varepsilon = \varepsilon_o\exp(\pm F_\pm/f_c)$, where ε_o is a constant and f_c is the characteristic load for detachment. To model the load $F_\pm$, we use a linear force–velocity relationship $F_\pm = \pm f_o(1 \mp \Delta_t/v_o)$,

3

Table 1. Filament/motor parameters reproduced from Oriola *et al.* [39] and Chakrabarti & Saintillan [40] and dimensionless parameters used in simulation.

dimensional		dimensionless	
L	50 μm	length scale (L)	
B	0.9–1.7 nN μm^2	force scale (B/L^2)	
τ_o	50 ms	time scale (τ_o)	
$\xi_\perp$	10^{-3}–1 Pa s	$Sp = L(\xi_\perp/B\tau_o)^{1/4}$	5–15
f_o	1–5 pN	$\mu_a = \rho a\, f_o\, L^2/B$	500–14000
f_c	0.5–2.5 pN	$f^* = f_o/f_c$	2
K	2×10^3 pN μm^{-2}	$\mu = a^2\, K\, L^2/B$	50
v_o	5–7 μm s^{-1}	$\zeta = a/v_o\tau_o$	0.4
a	200 nm	$\eta = \pi_o\tau_o$	0.14
ρ	10^3 μm^{-1}		

where Δ_t is the sliding velocity and f_o and v_o are the stall force and associated zero load velocity v_o at which the motors are at complete rest (see [39,40] and references therein for more details).

Put together, equations (2.16) that govern the fractions $n_\pm$ of motors bound to the ($\pm$) filaments become

$$(n_\pm)_t = \pi_o(1 - n_\pm) - \epsilon_o n_\pm \exp\left[\frac{f_o}{f_c}\left(1 \mp \frac{\Delta_t}{v_o}\right)\right], \tag{2.17}$$

and the resulting force $f(s, t)$ per unit length can be rewritten as

$$f(s, t) = \rho f_o\left[(n_+ - n_-) - (n_+ + n_-)\frac{\Delta_t}{v_o}\right] - K\Delta. \tag{2.18}$$

Equations (2.13), (2.17) and (2.18) need to be coupled to the filament equations, equations (2.5)–(2.7), via (2.14) to obtain a closed system of equations. Non-dimensional equations are obtained by considering the length scale of the filament L and the time scale $\tau_o = 1/(\pi_o + \epsilon_o)$ of the motor kinetics. Specifically, we define the sperm number $Sp^4 = f_h/f_e$, where $f_h = \xi_\perp L/\tau_o$ is the hydrodynamic force and $f_e = B/L^3$ is the elastic force due to bending. We also define the dimensionless active moment $\mu_a = m_a/m_e$, where $m_e = B/L^2$ is the elastic bending moment. Additional parameters include the stall to critical molecular force ratio $f^* = f_o/f_c$, the dimensionless sliding moment $\mu = a^2\, K/m_e$, the ratio $\zeta = a/v_o\tau_o$ of the cilium diameter a to the characteristic displacement $v_o\tau_o$ due to motor activity, and the duty ratio $\eta = \pi_o\tau_o$. Table 1 summarizes all dimensional and non-dimensional parameters.

Numerical solution of these nonlinear equations is obtained following Chakrabarti & Saintillan [40]. Namely, we discretize the arc length s with a second-order central difference method. At each time step, we first calculate the normal force and tension from the geometry. Then we apply a second-order accuracy explicit time stepping for θ, and an implicit Euler time stepping for $n_\pm$. Additional details on the numerical implementation can be found in appendix B.

3. Results

We first consider the model cilium with clamped boundary conditions. We vary the sperm number Sp and activity μ_a and examine the resulting beating patterns. Figure 2 shows
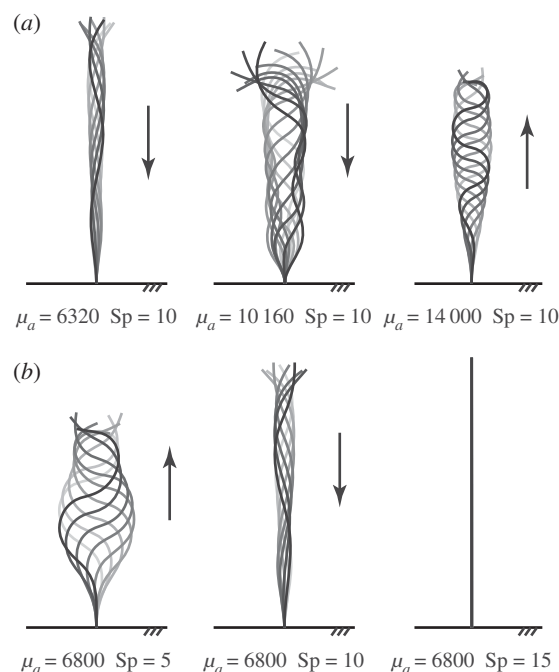

Figure 2. Model cilium waveforms. (*a*) As motor activity μ_a increases, the wave form changes its propagating direction from tip-to-base, to base-to-tip. (*b*) As sperm number Sp increases, the wave form changes back and eventually become stationary for large Sp. In all simulations, we used a mesh size $\Delta s = 0.01$ and an integration time step of $\Delta t = 3.125 \times 10^{-4}$.

that, for Sp = 10, as μ_a increases, the bending waves change from tip-to-base propagation to base-to-tip propagation, as reported in Chakrabarti & Saintillan [40]. All results are insensitive to initial conditions (see appendix C). For $\mu_a = 6800$, as Sp increases, the bending wave switches from base-to-tip propagation back to tip-to-base, and eventually remains stationary for large values of Sp. Increasing Sp is equivalent to increasing the cilium length, which, when holding all other parameters constant, leads to cases where activity is insufficient to trigger oscillations.

We next examine the relationship between the filament geometry and the dynein motor dynamics. According to equation (2.17), the dynein detachment rates $\varepsilon_\pm$ are governed by $\mp\Delta_t$. Figure 3 shows that changes in the sliding Δ correspond to the activation and inhibition of molecular motors along the + and − filaments. Specifically, the tip-to-base bending wave corresponds to a tip-to-base travelling wave in the motor activation dynamics $n_\pm$, and when the bending wave travels from base to tip, so does the motor activations. This is in accord with the experimental findings of Lin & Nicastro [12], where a 'switch-inhibition' mechanism was proposed.

For hinged boundary conditions (equation (2.11)), the model cilium produces a bending wave travelling from base to tip, consistent with the linearized analysis of Camalet & Jülicher [19], for all Sp and μ_a tested. Note that for small values of μ_a, the motor binding and unbinding dynamics switch between the + and − filaments with no prominent propagation of activity from base to tip (figure 4*a*). This implies that the base-to-tip bending waves are mostly due to elastohydrodynamics. For larger values of μ_a (figure 4*b*), the motor binding dynamics form wave patterns that travel from the base to its tip. Figure 4 also shows the formation of sharp propagation fronts (or shocks) in $n_\pm$. We numerically verified the existence of these solutions for distinct time steps
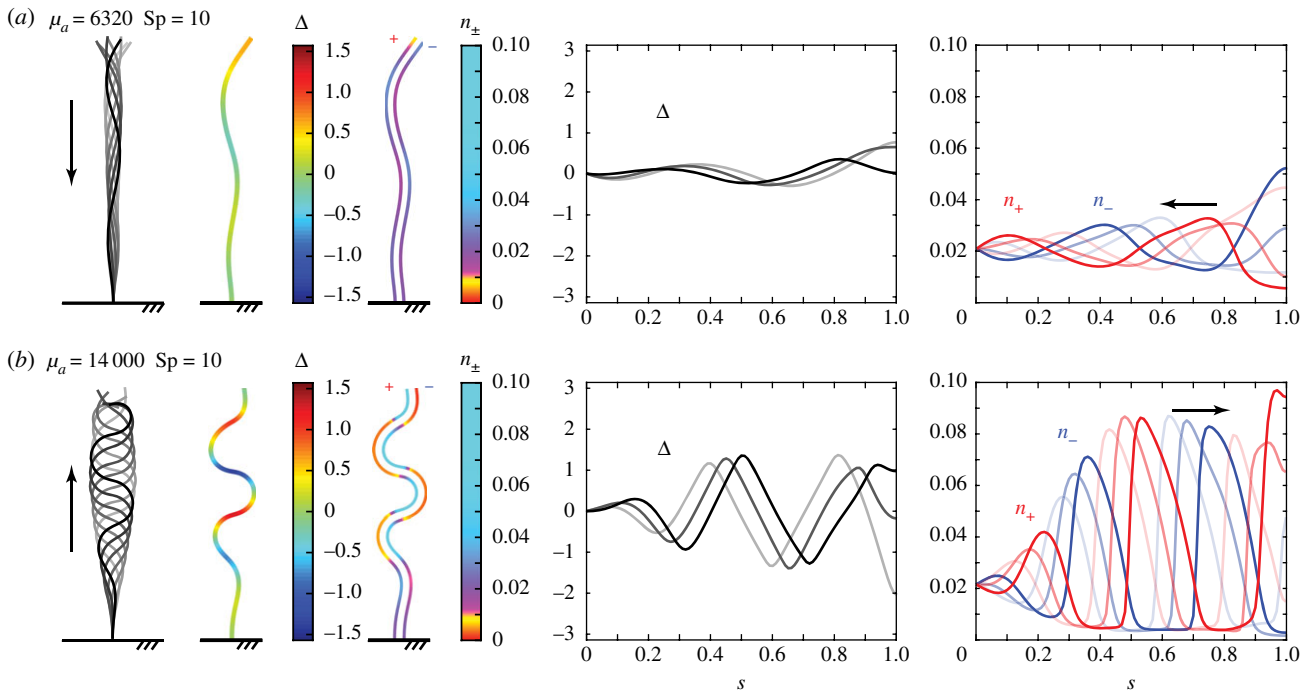
Figure 3. Motor switch-inhibition for clamped boundary condition. Snapshots of sliding magnitude Δ and dynein motor activities on $+$ and $-$ filaments, as well as the values of Δ, n_+, n_- along arc length at different times (opacity indicates passage of time). Row (a) shows example with tip-to-base waves at a small value of μ_a, while (b) shows that with base-to-tip waves after the second transition. Both examples have a clamped boundary condition at the base. In all simulations, we used a mesh size $\Delta s = 0.01$ and an integration time step of $\Delta t = 3.125 \times 10^{-4}$. (Online version in colour.)
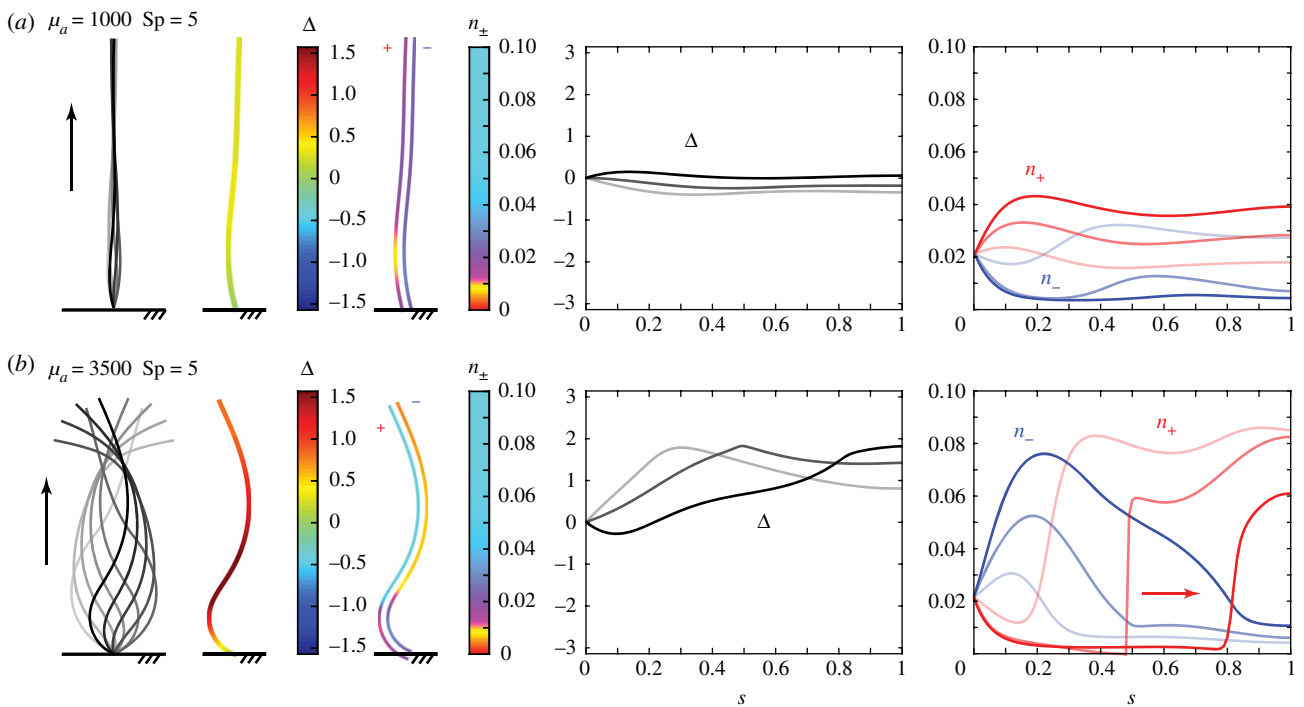

Figure 4. Motor switch-inhibition for hinged boundary condition. Snapshots of sliding magnitude Δ and motor activities on $+$ and $-$ filaments, as well as the values of Δ, n_+, n_- as functions of arc length at different times (opacity indicates passage of time). Row (a) shows results for a smaller value of motor activity μ_a. Both examples have bending waves travelling from base to tip, but at smaller μ_a, there is little propagation in $n_{\pm}$, thus the filament bending waves are attributed to elastohydrodynamics. In all simulations, we used a mesh size $\Delta s = 0.01$ and an integration time step of $\Delta t = 3.125 \times 10^{-4}$. (Online version in colour.)

(see appendix C). These sharp fronts imply that the molecular motor dynamics follow a nonlinear wave equation.

We analyse the behaviour of the clamped filament as a function of the parameter space Sp and μ_a. Analysis of hinged filament is omitted here because the direction of propagation of the bending waves does not change as we

vary these parameters. Specifically, in figure 5, we report the beating amplitude and frequency of oscillations for Sp = 5–15, $\mu_a = 2000$–14 000. We also report the evolution of the dominant eigenvalue based on linearized analysis (2.12) as a function of μ_a for Sp = 10. The linear stability results show an initial Hopf bifurcation leading to spontaneous
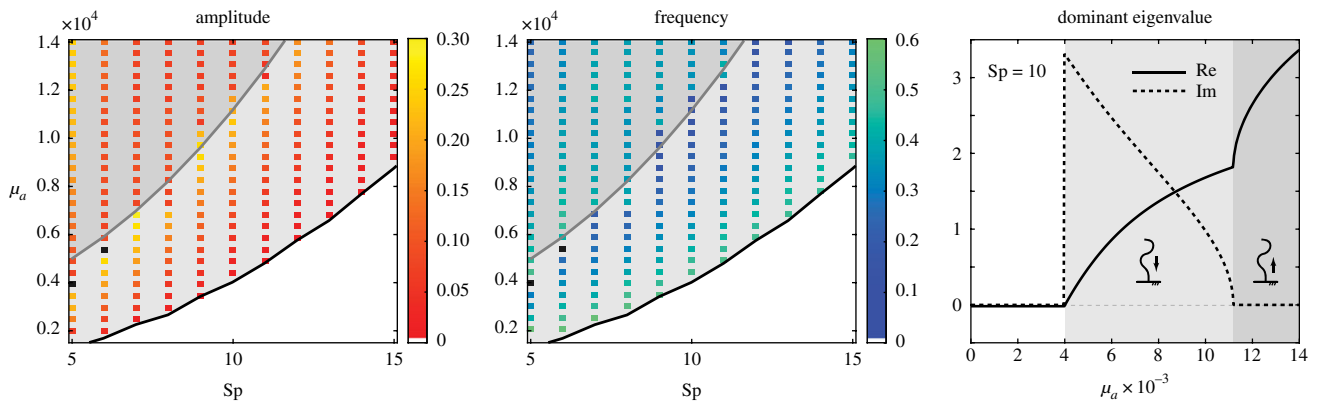
Figure 5. Analysis of sliding feedback control of dynein kinetics. Amplitude and frequency of oscillations. Amplitude is defined in the transverse (y) direction. Fundamental frequencies are obtained through autocorrelation of the time histories of the nonlinear waveform. Colours correspond to amplitude and frequency values as indicated by the colourbars to the right. Black squares indicate that multiple travelling or standing waves compete and a steady-state behaviour was not observed. Dominant eigenvalues from linear stability analysis are shown with respect to activity μ_a at Sp =10. The light grey region highlights the regime post the first bifurcation, where the filament undergoes spontaneous oscillation with tip-to-base bending waves. Dark grey indicates the regime post the second bifurcation where the filament bending waves travel from base to tip. In both regions, frequency *decreases* and amplitude *increases* with respect to *increase* in activity. Note that sperm number shown is normalized with respect to drag coefficient $\xi_\perp$ (instead of fluid viscosity in [40]). In all simulations, we used a mesh size $\Delta s = 0.01$ and an integration time step of $\Delta t = 3.125 \times 10^{-4}$. (Online version in colour.)

oscillations from tip to base, and a second transition leading to base-to-tip travelling waves, as reported in Chakrabarti & Saintillan [40]. A close examination of the amplitude and frequency of oscillations across these transitions (delineated by solid lines) in the left two panels of figure 5, shows the following: (i) there is a jump or discontinuity in amplitude and frequency at the second transition when bending waves change the direction of propagation, and (ii) in both regimes, the amplitude of oscillations increase with increasing activity and the frequency decreases. This is in contrast to experimental observations where an increase in ATP concentration (for which μ_a is a proxy) correspond to saturated growth in both beating amplitudes and frequencies [10].

4. Discussion

We revisited a model of cilia oscillations with sliding feedback control [39,40], and examined differences in filament dynamics with respect to different boundary conditions. As the activity level increases, the model exhibits a Hopf bifurcation that leads to sustained oscillations. The direction of deformation waves depends on the boundary conditions. For hinged boundary conditions, the waves propagate from base to tip only. For clamped boundary conditions, the waves propagate from tip to base following this Hopf bifurcation, and a second bifurcation exists at higher activity levels leading to reversal in wave propagation from tip-to-base to base-to-tip.

The exact mechanical conditions at the base of cilia and flagella are very complex. Cilia from different cell types can originate from basal bodies with diverse structural details [54]. The realistic boundary conditions at the base of cilia are probably in between the ideal cases of clamped and hinged filaments, and are likely to vary between organisms and during the different stages of development. The two cases studied here serve to highlight the subtle effects of the mechanical conditions at the boundary on filament oscillations.

Certain microorganisms of the order Trypanosomatida are known to control the direction of flagellar beat propagation [55–58]. The model suggests that sliding motor control could enable such wave reversal for clamped filaments. Further, the model generates bending waves that are correlated with switch-inhibition of motor activation similar to experimental observations [12]. However, other evidence points to the incompleteness of this sliding control model. In the model, the oscillation amplitude increases with increasing motor activity and the frequency decreases. These trends are in striking contrast to experimental observations of cilia, where the oscillation amplitude and frequency undergo saturated growth with increasing ATP levels [10]. Moreover, in this sliding feedback model, the waveforms differ from the beating patterns observed in cilia. To produce cilia-like oscillations, Chakrabarti & Saintillan [40] introduced curvature control and bias in the molecular motor kinetics. The mechano-chemical processes that would form the basis of such bias are not clear. Based on these discrepancies, we are inclined to conclude that the sliding feedback control, although it may play a role in the molecular motor kinetics, is unlikely to be the only mechanism driving cilia oscillations.

To date, mathematical models of cilia have generated a gallery of potential mechanisms that can lead to sustained oscillations. Recent studies have begun to address the relative merits of these candidate mechanisms in comparison to experiments [36,59–64]. However, at present, there is no experimental benchmark of cilia oscillations under agreed upon 'nominal' and 'altered' conditions that can be used as a testbed for theoretical models. To evaluate mathematical models, we need to compare their behaviour to experimental results, but, more importantly, we need to test their predictive ability under altered conditions. The analysis presented in Bottier *et al.* [60] of oscillation frequency versus cilium length in the Chlamydomonas is an example. Four theoretical models were tested in Bottier *et al.* [60], none of which was able to reproduce the experimentally observed trends in frequency versus length. Until we, as a community, establish clear experimental benchmarks that can be used to scrutinize theoretical models for their ability to reproduce cilia beating patterns and to predict changes in these patterns under altered conditions, the regulation of molecular motor activity in cilia oscillations remains an open problem.

Appendix A. Linearization

The dimensionless nonlinear equations are of the form (using $\gamma = \xi_\parallel/\xi_\perp = 1/2$)

$$0 = \sigma_{ss} - \frac{3}{2}N_s\theta_s - N\theta_{ss} - \frac{1}{2}\sigma\theta_s^2, \tag{A 1}$$

$$\mathrm{Sp}^4\theta_t = N_{ss} - 2N\theta_s^2 + 3\sigma_s\theta_s + \sigma\theta_{ss}, \tag{A 2}$$

$$0 = \theta_{ss} + N + \mu_a f, \tag{A 3}$$

$$f = (n_+ - n_-) - \zeta\theta_t(n_+ + n_-) - \frac{\mu}{\mu_a}\theta \tag{A 4}$$

and

$$
\begin{aligned}
(\partial n_\pm)_t &= \eta(1 - n_\pm) \\
&- (1 - \eta)n_\pm \exp[f^*(1 \mp \zeta\theta_t)].
\end{aligned} \tag{A 5}
$$

When the filament is clamped at the base, the nonlinear boundary conditions are

$$\theta|_{s=0} = 0, \quad (\sigma\theta_s + N_s)|_{s=0} = 0, \quad (\sigma_s - N\theta_s)|_{s=0} = 0 \tag{A 6}$$

and

$$\theta_s|_{s=1} = 0, \quad \sigma|_{s=1} = 0, \quad N|_{s=1} = 0. \tag{A 7}$$

Assuming small displacement around the straight filament configuration ($\theta = \delta\theta$), we can linearize equations (A 1)–(A 3) and obtain the following linear equations for the filament:

$$\mathrm{Sp}^4\theta_t = N_{ss} \tag{A 8}$$

and

$$N = \mu\theta - \theta_{ss} - \mu_a[(n_+ - n_-) - \zeta\theta_t(n_+ + n_-)]. \tag{A 9}$$

Since the equilibrium solution of $n_\pm$ is $n_o = \eta/(\eta + (1 - \eta)e^{f^*})$, we can obtain the leading-order equation for motor states by substituting $n_\pm = n_o \pm \delta n$ into equation (A 5) and get

$$\delta n_t = -[\eta + (1 - \eta)e^{f^*}]\delta n + (1 - \eta)f^*e^{f^*}\zeta n_o\theta_t. \tag{A 10}$$

Equation (2.12) of main text can be thus obtained by substituting equation (A 9) into (A 8). But for the purpose of computing dominant eigenvalues shown in figure 5, we can linearize the boundary conditions and get

$$\theta|_{s=0} = 0, \quad N_s|_{s=0} = 0 \tag{A 11}$$

and

$$\theta_s|_{s=1} = 0, \quad N|_{s=1} = 0. \tag{A 12}$$

for the clamped case, and solve equations (A 8) and (A 9) directly after discretization of the spatial derivatives.

Appendix B. Numerical method

Following Chakrabarti & Saintillan [40], we discretize the arc length s uniformly with $M + 1$ points, with mesh size $\Delta s = 1/M$. We use the second-order central difference formula for the spatial derivatives

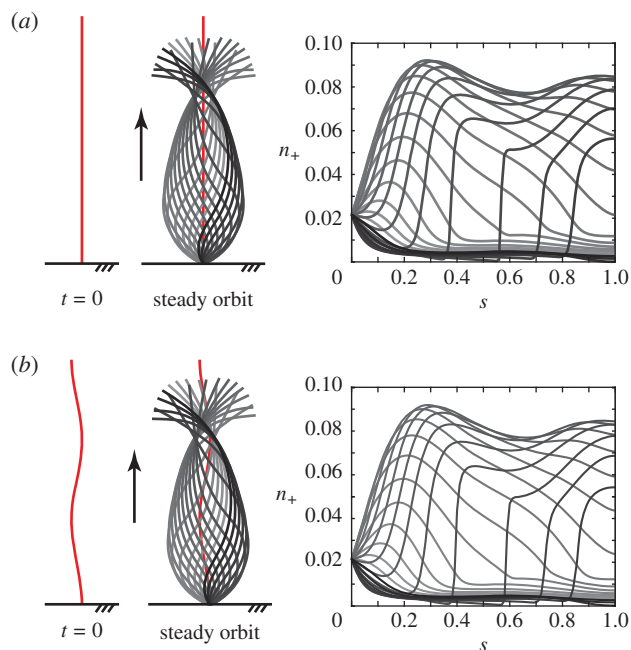$$(\cdot)_{s,j} \simeq \frac{1}{2\Delta s}[-(\cdot)_{j-1} + (\cdot)_{j+1}] \tag{B 1}$$

Figure 6. Robustness to initial conditions. Initial values (red) for **r** and final steady orbit (greyscale) of **r** and n_+ before $T = 25$ are shown for two different initial conditions. Initial conditions for motor states are always chosen to be constant with respect to s (not shown). In (*a*), we start from an almost straight configuration except that the midpoint is perturbed slightly, $\theta(s = 0.5, t = 0) = 0.001$. In (*b*), the initial condition for θ is set to be $0.2\sin(3\pi s)$. It is clear that resultant steady orbit for both θ and n_+ are identical, except that due to the hinged boundary condition, the mean angular position of the final periodic solution is determined by that of the initial condition. In both cases, the motor state n_+ exhibit identical sharp wave front propagation from base to tip. Here we used Sp =5 and $\mu_a = 3500$, identical to figure 4*b* in the main text. We also used a mesh size $\Delta s = 0.01$ and an integration time step of $\Delta t = 3.125 \times 10^{-4}$. (Online version in colour.)

and

$$(\cdot)_{ss,j} \simeq \frac{1}{\Delta s^2}[(\cdot)_{j-1} - 2(\cdot)_j + (\cdot)_{j+1}]. \tag{B 2}$$

We use second-order forward and backward difference formula to enforce the base and tip boundary conditions, respectively.

To obtain nonlinear solutions for θ, we first substitute equations (A 2) and (A 4) into (A 3) and obtain

$$
\begin{aligned}
\mathrm{Sp}^4[\mu_a(n_+ - n_-) &- \mu\theta + \theta_{ss} + N] \\
&= \mu_a\zeta(n_+ + n_-)[N_{ss} - 2N\theta_s^2 + 3\sigma_s\theta_s + \sigma\theta_{ss}]. \tag{B 3}
\end{aligned}
$$

Then at each time step k, we first calculate the normal force $N^{(k)}$ and tension $\sigma^{(k)}$ using equations (A 1) and (B 3). We then enforce boundary conditions for $\sigma^{(k)}$ and $N^{(k)}$ using $\theta^{(k-1)}$. Next, we employ a second-order backward scheme to equation (A 2) and get

$$
\begin{aligned}
\frac{\mathrm{Sp}^4}{2\Delta t}[3\theta^{(k+1)} &- 4\theta^{(k)} + \theta^{(k-1)}] \\
&= N_{ss}^{(k)} - 2N^{(k)}(\theta_s^{(k)})^2 + 3\sigma_s^{(k)}\theta_s^{(k)} + \sigma^{(k)}\theta_{ss}^{(k)}. \tag{B 4}
\end{aligned}
$$

We enforce the boundary conditions for $\theta^{(k)}$ at this step. Finally,

7

royalsocietypublishing.org/journal/rstb   *Phil. Trans. R. Soc. B* **375**: 20190157
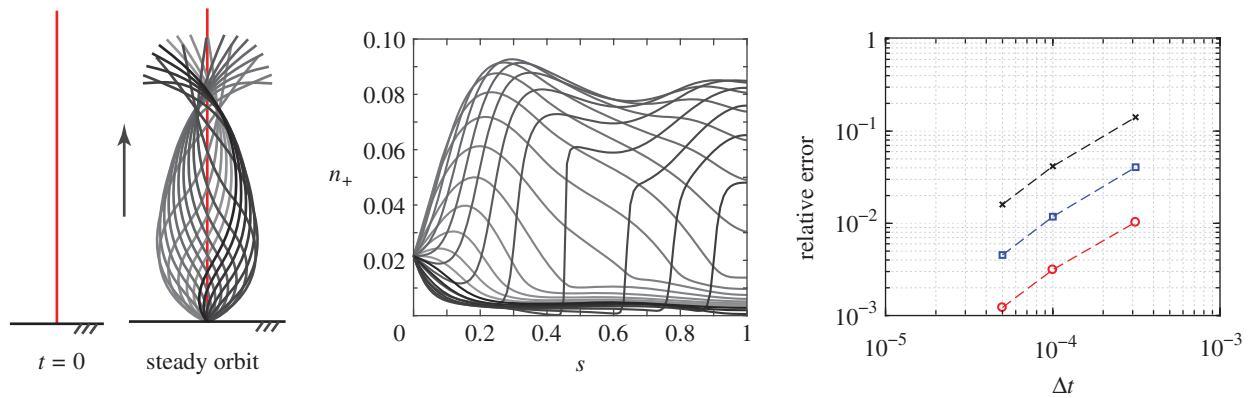
Figure 7. Convergence of numerical sharp wave front solution. The almost straight initial condition (red) for $\mathbf{r}$ and final steady orbit (greyscale) of $\mathbf{r}$ and n_+ are shown next to each other for $\Delta t = 10^{-4}$. The relative error (L2 norm) of the final solution at $T = 25$ at various Δt and fixed mesh size $\Delta s = 0.01$ is computed against $\Delta t = 2 \times 10^{-5}$ and shown on the right. Black crosses are relative error of position $\mathbf{r}$, whereas red circles and blue squares represent that of motor state n_+ and n_-, respectively. It is evident that the numerical method is converging to a consistent solution, where a sharp wave front propagates from base to tip for $n_\pm$. Here we used Sp $=5$ and $\mu_a = 3500$, identical to figure 4b in the main text. (Online version in colour.)

we use the implicit Euler scheme on equation (A 5) to get

$$\frac{1}{\Delta t}[n_\pm^{(k+1)} - n_\pm^{(k)}]$$
$$= \eta[1 - n_\pm^{(k+1)}] - (1 - \eta)n_\pm^{(k+1)} \exp[f^*(1 \mp \zeta\theta_t^{(k)})], \quad \text{(B 5)}$$

where $\theta_t^{(k)} = \Delta t^{-1}[\theta^{(k+1)} - \theta^{(k)}]$.

When solving for the hinged boundary condition, we replace the first formula in equation (A 6) with

$$\theta_s|_{s=0} - \mu_a \int_0^1 f(s', t)\,ds' = 0. \quad \text{(B 6)}$$

Substituting equations (A 3) into (B 6), we get

$$\theta_s|_{s=0} - \mu_a \int_0^1 f(s', t)\,ds' = \theta_s|_{s=0} + \int_0^1 (\theta_{ss} + N)ds'$$
$$= \theta_s|_{s=0} - \theta_s|_{s=0} + \int_0^1 N\,ds,$$
$$= \int_0^1 N\,ds, \quad \text{(B 7)}$$

where we used the boundary condition $\theta_s|_{s=1} = 0$. We arrive at

$$\int_0^1 N\,ds = 0. \quad \text{(B 8)}$$

This constraint needs to be enforced when solving for the normal and tensile components of the force via equations (A 1) and (B 3). The discretized version of this integral constraint is

$$\frac{1}{2}N_1 + \sum_{j=2}^M N_j + \frac{1}{2}N_{M+1} = 0. \quad \text{(B 9)}$$

All other equations follow the same form as in the clamped case.

Appendix C. Numerical validations

We have verified that our results for the clamped boundary conditions are similar to those reported in Oriola et al. [39] and Chakrabarti & Saintillan [40]. Here, we present our validation results for the hinged boundary condition only. We choose the case shown in figure 4 of the main text as our test case. In figure 6, we use two distinct initial conditions and show that the filament behaviour is robust to variations in initial conditions. In figure 7, we vary the integration time step and show that the filament behaviour and molecular motor dynamics are robust to the integration time step. All simulations of this work; we choose a mesh size $\Delta s = 0.01$ and an integration time step of $\Delta t = 3.125 \times 10^{-4}$.

References

1. Satir P, Sleigh MA. 1990 The physiology of cilia and mucociliary interactions. *Ann. Rev. Physiol.* **52**, 137–155. (doi:10.1146/annurev.ph.52.030190.001033)

2. Satir P, Christensen ST. 2007 Overview of structure and function of mammalian cilia. *Ann. Rev. Physiol.* **69**, 377–400. (doi:10.1146/annurev.physiol.69.040705.141236)

3. Woolley D. 1975 The rat sperm tail after fixation by freeze-substitution. In *The functional anatomy of the spermatozoon: Proc. 2nd Int. Symp. Wenner-Gren Center, Stockholm, August 1973*, vol. 23, p. 177. Oxford, UK: Pergamon.

4. Gibbons BH, Gibbons I. 1974 Properties of flagellar 'rigor waves' formed by abrupt removal of adenosine triphosphate from actively swimming sea urchin sperm. *J. Cell Biol.* **63**, 970–985. (doi:10.1083/jcb.63.3.970)

5. Goldstein SF. 1979 Starting transients in sea urchin sperm flagella. *J. Cell Biol.* **80**, 61–68. (doi:10.1083/jcb.80.1.61)

6. Gibbons I. 1981 Cilia and flagella of eukaryotes. *J. Cell Biol.* **91**, 107s–124s. (doi:10.1083/jcb.91.3.107s)

7. Movassagh T, Bui KH, Sakakibara H, Oiwa K, Ishikawa T. 2010 Nucleotide-induced global conformational changes of flagellar dynein arms revealed by in situ analysis. *Nat. Struct. Mol. Biol.* **17**, 761. (doi:10.1038/nsmb.1832)

8. Lin J, Tritschler D, Song K, Barber CF, Cobb JS, Porter ME, Nicastro D. 2011 Building blocks of the nexin-dynein regulatory complex in *Chlamydomonas* flagella. *J. Biol. Chem.* **286**, 29 175–29 191. (doi:10.1074/jbc.M111.241760)

9. Lin J, Okada K, Raytchev M, Smith MC, Nicastro D. 2014 Structural mechanism of the dynein power stroke. *Nat. Cell Biol.* **16**, 479. (doi:10.1038/ncb2939)

10. Chen DT, Heymann M, Fraden S, Nicastro D, Dogic Z. 2015 ATP consumption of eukaryotic flagella measured at a single-cell level. *Biophys. J.* **109**, 2562–2573. (doi:10.1016/j.bpj.2015.11.003)

11. Geyer VF, Sartori P, Friedrich BM, Jülicher F, Howard J. 2016 Independent control of the static and dynamic

components of the *Chlamydomonas* flagellar beat. *Curr. Biol.* **26**, 1098–1103. (doi:10.1016/j.cub.2016.02.053)

12. Lin J, Nicastro D. 2018 Asymmetric distribution and spatial switching of dynein activity generates ciliary motility. *Science* **360**, eaar1968. (doi:10.1126/science.aar1968)

13. Tani T, Kamimura S. 1998 Reactivation of sea-urchin sperm flagella induced by rapid photolysis of caged ATP. *J. Exp. Biol.* **201**, 1493–1503.

14. Brokaw CJ. 1994 Control of flagellar bending: a new agenda based on dynein diversity. *Cell Motil. Cytoskeleton* **28**, 199–204. (doi:10.1002/cm.970280303)

15. Mukundan V, Sartori P, Geyer V, Jülicher F, Howard J. 2014 Motor regulation results in distal forces that bend partially disintegrated *Chlamydomonas* axonemes into circular arcs. *Biophys. J.* **106**, 2434–2442. (doi:10.1016/j.bpj.2014.03.046)

16. Jülicher F, Prost J. 1995 Cooperative molecular motors. *Phys. Rev. Lett.* **75**, 2618. (doi:10.1103/PhysRevLett.75.2618)

17. Brokaw CJ. 1966 Bend propagation along flagella. *Nature* **209**, 161. (doi:10.1038/209161a0)

18. Hines M, Blum J. 1978 Bend propagation in flagella. I. Derivation of equations of motion and their simulation. *Biophys. J.* **23**, 41–57. (doi:10.1016/S0006-3495(78)85431-9)

19. Camalet S, Jülicher F. 2000 Generic aspects of axonemal beating. *New J. Phys.* **2**, 24. (doi:10.1088/1367-2630/2/1/324)

20. Lindemann CB. 1994 A model of flagellar and ciliary functioning which uses the forces transverse to the axoneme as the regulator of dynein activation. *Cell Motil. Cytoskeleton* **29**, 141–154. (doi:10.1002/cm.970290206)

21. Lindemann CB. 1994 A 'geometric clutch' hypothesis to explain oscillations of the axoneme of cilia and flagella. *J. Theor. Biol.* **168**, 175–189. (doi:10.1006/jtbi.1994.1097)

22. Lindemann CB. 2002 Geometric clutch model version 3: the role of the inner and outer arm dyneins in the ciliary beat. *Cell Motil. Cytoskeleton* **52**, 242–254. (doi:10.1002/cm.10049)

23. Dillon RH, Fauci LJ. 2000 An integrative model of internal axoneme mechanics and external fluid dynamics in ciliary beating. *J. Theor. Biol.* **207**, 415–430. (doi:10.1006/jtbi.2000.2182)

24. Dillon RH, Fauci LJ, Omoto C. 2003 Mathematical modeling of axoneme mechanics and fluid dynamics in ciliary and sperm motility. *Dyn. Contin. Discrete Impulsive Syst. Ser. A* **10**, 745–758.

25. Hilfinger A, Riedel-Kruse I, Howard J, Jülicher F. 2009 How molecular motors shape the flagellar beat. *Biophys. J.* **96**, 196a. (doi:10.1016/j.bpj.2008.12.1051)

26. Bayly PV, Wilson KS. 2015 Analysis of unstable modes distinguishes mathematical models of flagellar motion. *J. R. Soc. Interface* **12**, 20150124. (doi:10.1098/rsif.2015.0124)

27. Goldstein RE, Lauga E, Pesci AI, Proctor MR. 2016 Elastohydrodynamic synchronization of adjacent beating flagella. *Phys. Rev. Fluids* **1**, 073201. (doi:10.1103/PhysRevFluids.1.073201)

28. Han J, Peskin CS. 2018 Spontaneous oscillation and fluid–structure interaction of cilia. *Proc. Natl*

Acad. Sci. USA **115**, 4417–4422. (doi:10.1073/pnas.1712042115)

29. Guo H, Fauci L, Shelley MJ, Kanso E. 2018 Bistability in the synchronization of actuated microfilaments. *J. Fluid Mech.* **836**, 304–323. (doi:10.1017/jfm.2017.816)

30. Bayly PV, Dutcher S. 2016 Steady dynein forces induce flutter instability and propagating waves in mathematical models of flagella. *J. R. Soc. Interface* **13**, 20160523. (doi:10.1098/rsif.2016.0523)

31. Hu T, Bayly PV. 2018 Finite element models of flagella with sliding radial spokes and interdoublet links exhibit propagating waves under steady dynein loading. *Cytoskeleton* **75**, 185–200. (doi:10.1002/cm.21432)

32. Ling F, Guo H, Kanso E. 2018 Instability-driven oscillations of elastic microfilaments. *J. R. Soc. Interface* **15**, 20180594. (doi:10.1098/rsif.2018.0594)

33. Brokaw CJ. 1971 Bend propagation by a sliding filament model for flagella. *J. Exp. Biol.* **55**, 289–304.

34. Hilfinger A, Chattopadhyay AK, Jülicher F. 2009 Nonlinear dynamics of cilia and flagella. *Phys. Rev. E* **79**, 051918. (doi:10.1103/PhysRevE.79.051918)

35. Bayly PV, Wilson KS. 2014 Equations of interdoublet separation during flagella motion reveal mechanisms of wave propagation and instability. *Biophys. J.* **107**, 1756–1772. (doi:10.1016/j.bpj.2014.07.064)

36. Sartori P, Geyer VF, Scholich A, Jülicher F, Howard J. 2016 Dynamic curvature regulation accounts for the symmetric and asymmetric beats of *Chlamydomonas* flagella. *Elife* **5**, e13258. (doi:10.7554/eLife.13258)

37. Sartori P, Geyer VF, Howard J, Jülicher F. 2016 Curvature regulation of the ciliary beat through axonemal twist. *Phys. Rev. E* **94**, 042426. (doi:10.1103/PhysRevE.94.042426)

38. De Canio G, Lauga E, Goldstein RE. 2017 Spontaneous oscillations of elastic filaments induced by molecular motors. *J. R. Soc. Interface* **14**, 20170491. (doi:10.1098/rsif.2017.0491)

39. Oriola D, Gadêlha H, Casademunt J. 2017 Nonlinear amplitude dynamics in flagellar beating. *R. Soc. open sci.* **4**, 160698. (doi:10.1098/rsos.160698)

40. Chakrabarti B, Saintillan D. 2019 Spontaneous oscillations, beating patterns, and hydrodynamics of active microfilaments. *Phys. Rev. Fluids* **4**, 043102. (doi:10.1103/PhysRevFluids.4.043102)

41. Machin K. 1958 Wave propagation along flagella. *J. Exp. Biol.* **35**, 796–806.

42. Wiggins CH, Riveline D, Ott A, Goldstein RE. 1998 Trapping and wiggling: elastohydrodynamics of driven microfilaments. *Biophys. J.* **74**, 1043–1060. (doi:10.1016/S0006-3495(98)74029-9)

43. Gray J, Hancock G. 1955 The propulsion of sea-urchin spermatozoa. *J. Exp. Biol.* **32**, 802–814.

44. Lauga E, Powers TR. 2009 The hydrodynamics of swimming microorganisms. *Rep. Prog. Phys.* **72**, 096601. (doi:10.1088/0034-4885/72/9/096601)

45. Johnson RE. 1980 An improved slender-body theory for Stokes flow. *J. Fluid Mech.* **99**, 411–431. (doi:10.1017/S0022112080000687)

46. Lighthill J. 1976 Flagellar hydrodynamics. *SIAM Rev.* **18**, 161–230. (doi:10.1137/1018040)

47. Cox R. 1970 The motion of long slender bodies in a viscous fluid part 1. General theory. *J. Fluid Mech.* **44**, 791–810. (doi:10.1017/S002211207000215X)

48. Keller JB, Rubinow SI. 1976 Slender-body theory for slow viscous flow. *J. Fluid Mech.* **75**, 705–714. (doi:10.1017/S0022112076000475)

49. Lindemann CB, Macauley LJ, Lesich KA. 2005 The counterbend phenomenon in dynein-disabled rat sperm flagella and what it reveals about the interdoublet elasticity. *Biophys. J.* **89**, 1165–1174. (doi:10.1529/biophysj.105.060681)

50. Gadêlha H, Gaffney EA, Goriely A. 2013 The counterbend phenomenon in flagellar axonemes and cross-linked filament bundles. *Proc. Natl Acad. Sci. USA* **110**, 12 180–12 185. (doi:10.1073/pnas.1302113110)

51. Lesich KA, Pelle DW, Lindemann CB. 2016 Mechanics of the eukaryotic flagellar axoneme: evidence for structural distortion during bending. *Cytoskeleton* **73**, 233–245. (doi:10.1002/cm.21296)

52. Coy R, Gadêlha H. 2017 The counterbend dynamics of cross-linked filament bundles and flagella. *J. R. Soc. Interface* **14**, 20170065. (doi:10.1098/rsif.2017.0065)

53. Jülicher F, Prost J. 1997 Spontaneous oscillations of collective molecular motors. *Phys. Rev. Lett.* **78**, 4510. (doi:10.1103/PhysRevLett.78.4510)

54. Fawcett DW, Porter KR. 1954 A study of the fine structure of ciliated epithelia. *J. Morphol.* **94**, 221–281. (doi:10.1002/jmor.1050940202)

55. Gittleson SM. 1974 Flagellar activity and Reynolds number. *Trans. Am. Microsc. Soc.* **93**, 272–276. (doi:10.2307/3225301)

56. Baron DM, Kabututu ZP, Hill KL. 2007 Stuck in reverse: loss of LC1 in *Trypanosoma brucei* disrupts outer dynein arms and leads to reverse flagellar beat and backward movement. *J. Cell Sci.* **120**, 1513–1520. (doi:10.1242/jcs.004846)

57. Gadelha C, Wickstead B, Gull K. 2007 Flagellar and ciliary beating in trypanosome motility. *Cell Motil. Cytoskeleton* **64**, 629–643. (doi:10.1002/cm.20210)

58. Wheeler RJ. 2017 Use of chiral cell shape to ensure highly directional swimming in trypanosomes. *PLoS Comput. Biol.* **13**, e1005353. (doi:10.1371/journal.pcbi.1005353)

59. Riedel-Kruse IH, Müller C, Oates AC. 2007 Synchrony dynamics during initiation, failure, and rescue of the segmentation clock. *Science* **317**, 1911–1915. (doi:10.1126/science.1142538)

60. Bottier M, Thomas KA, Dutcher SK, Bayly PV. 2019 How does cilium length affect beating? *Biophys. J.* **116**, 1292–1304. (doi:10.1016/j.bpj.2019.02.012)

61. Lindemann CB, Lesich KA. 2015 The geometric clutch at 20: stripping gears or gaining traction? *Reproduction* **150**, R45–R53. (doi:10.1530/REP-14-0498)

62. Brokaw CJ. 2009 Thinking about flagellar oscillation. *Cell Motil. Cytoskeleton* **66**, 425–436. (doi:10.1002/cm.20313)

63. Woolley DM. 2010 Flagellar oscillation: a commentary on proposed mechanisms. *Biol. Rev. Camb. Philos. Soc.* **85**, 453–470. (doi:10.1111/j.1469-185X.2009.00110.x)

64. Lindemann CB, Lesich KA. 2010 Flagellar and ciliary beating: the proven and the possible. *J. Cell Sci.* **123**, 519–528. (doi:10.1242/jcs.051326)